



Nanocrystalline $\text{CaSb}_2\text{O}_5(\text{OH})_2$ and $\text{Ca}_2\text{Sb}_2\text{O}_7$: Controlled syntheses, electronic structures and photocatalytic activity

Renkun Huang^a, Ximing Xu^a, Jia Zhu^b, Wenjun Liu^a, Rusheng Yuan^a, Xianzhi Fu^a, Yongfan Zhang^{b,*}, Zhaohui Li^{a,*}

^a Research Institute of Photocatalysis, Fujian Provincial Key Laboratory of Photocatalysis – State Key Laboratory Breeding Base, Fuzhou University, Fuzhou 350002, PR China

^b Department of Chemistry, Fuzhou University, Fuzhou, Fujian 350108, PR China

ARTICLE INFO

Article history:

Received 31 May 2012

Received in revised form 15 August 2012

Accepted 26 August 2012

Available online 31 August 2012

Keywords:

Hydrothermal

Photocatalysis

Electronic structure

Crystal structure

ABSTRACT

A facile one-pot pH-dependent hydrothermal method has been developed in the controlled syntheses of $\text{CaSb}_2\text{O}_5(\text{OH})_2$ and cubic $\text{Ca}_2\text{Sb}_2\text{O}_7$ with large specific surface area. The as-obtained samples were characterized by X-ray diffraction (XRD), N_2 -sorption BET surface area, UV-vis diffuse reflectance spectroscopy (DRS), transmission electron microscopy (TEM), high-resolution transmission electron microscopy (HRTEM), energy dispersive X-ray analysis (EDX) and Fourier transformation infrared spectroscopy (FT-IR). The electronic structures of $\text{CaSb}_2\text{O}_5(\text{OH})_2$ and cubic $\text{Ca}_2\text{Sb}_2\text{O}_7$ were determined by density functional theory (DFT) calculations. The photocatalytic performance of the as-prepared $\text{CaSb}_2\text{O}_5(\text{OH})_2$ and cubic $\text{Ca}_2\text{Sb}_2\text{O}_7$ was evaluated by the degradation of methyl orange (MO) and gaseous benzene. It was found that $\text{CaSb}_2\text{O}_5(\text{OH})_2$ is more photocatalytic active than $\text{Ca}_2\text{Sb}_2\text{O}_7$. A low crystal packing factor (PF) of $\text{CaSb}_2\text{O}_5(\text{OH})_2$ is probably responsible for its superior photocatalytic performance as compared to that of cubic $\text{Ca}_2\text{Sb}_2\text{O}_7$.

© 2012 Elsevier B.V. All rights reserved.

1. Introduction

Semiconductor-based photocatalytic oxidation has been established to be one of the most promising technologies for the environment remediation and has been employed in the treatment of all kinds of organic contaminants [1–3]. The effective application of photocatalysis in environmental remediation requires that the photocatalysts should be of high photocatalytic efficiency. Therefore during the past decade, tremendous effort has been devoted to the development of new photocatalysts [4–11]. In addition to TiO_2 -based photocatalysts, many non- TiO_2 photocatalysts based on single-phase-oxide have been developed so far. However, some photocatalysts lack the long-term stability, while some show low activity, or require rigorous synthetic condition. The development of new photocatalyst with high performance is still a great challenge in photocatalysis so far.

Recently metal oxides with distorted Sb–O polyhedra in their structures, like $\text{M}_2\text{Sb}_2\text{O}_7$ ($\text{M}=\text{Sr}^{2+}$ and Ca^{2+}) [12,13], PbSb_2O_6 [14], BiSbO_4 [15,16], MSb_2O_6 ($\text{M}=\text{Ca}$, Sr and Ba) [17] and ZnSb_2O_6 [18], have been found to be photocatalytic active. Among them, Ca–Sb oxide $\text{Ca}_2\text{Sb}_2\text{O}_7$ in orthorhombic phase and oxyhydroxide

$\text{CaSb}_2\text{O}_5(\text{OH})_2$ have both been reported to show photocatalytic activity for the degradations of dyes and benzene [12,19]. In addition to orthorhombic phase, $\text{Ca}_2\text{Sb}_2\text{O}_7$ exists in another polymorphism as cubic phase. However, there is no report on the photocatalytic performance over cubic $\text{Ca}_2\text{Sb}_2\text{O}_7$. Since different polymorphs of inorganic materials usually exhibit different properties, and examples that photocatalysts with different crystal phase behave quite differently have been well documented, it is therefore interesting to explore the photocatalytic performance of the cubic $\text{Ca}_2\text{Sb}_2\text{O}_7$.

The already reported methods for the preparations of Ca–Sb oxide and oxyhydroxide include the solid state reaction, ion-exchange and microwave-assisted hydrothermal method [12,19,20]. However, samples obtained from the solid state reaction usually suffer from problems such as excessive crystal growth, small BET specific surface area, etc. All these would lead to inferior photocatalytic activity. Ion-exchange is complicated and time-consuming while microwave-assisted hydrothermal method requires the specific apparatus and involves with starting material which is difficult to handle. For the applications of Ca–Sb oxide and oxyhydroxide in the photocatalysis, it is therefore preferable that a facile method should be developed to prepare nanocrystalline samples with large specific surface area via cheap commercial starting material.

In this manuscript, we reported the pH-dependent controlled syntheses of $\text{CaSb}_2\text{O}_5(\text{OH})_2$ and cubic phase $\text{Ca}_2\text{Sb}_2\text{O}_7$ from Sb_2O_5

* Corresponding authors.

E-mail addresses: zhangyf@fzu.edu.cn (Y. Zhang), zhaohuili1969@yahoo.com (Z. Li).

via a facile hydrothermal method. The electronic structure of $\text{CaSb}_2\text{O}_5(\text{OH})_2$ and cubic $\text{Ca}_2\text{Sb}_2\text{O}_7$ were determined by DFT calculations. The photocatalytic performance of the hydrothermal prepared $\text{CaSb}_2\text{O}_5(\text{OH})_2$ and $\text{Ca}_2\text{Sb}_2\text{O}_7$ was evaluated by the degradation of methyl orange (MO) and gaseous benzene. The different photocatalytic activity of $\text{CaSb}_2\text{O}_5(\text{OH})_2$ and $\text{Ca}_2\text{Sb}_2\text{O}_7$ is discussed in terms of their different crystal structure.

2. Experimental

2.1. Syntheses

All reagents were analytical grade and used without further purifications. Nanocrystalline $\text{Ca}(\text{CH}_3\text{COO})_2 \cdot \text{H}_2\text{O}$ and Sb_2O_5 were used as starting materials. In a typical procedure, Sb_2O_5 powder (0.809 g, 2.5 mmol) and $\text{Ca}(\text{CH}_3\text{COO})_2 \cdot \text{H}_2\text{O}$ (0.441 g, 2.5 mmol) were mixed in 12 mL deionized water. The pH of the resulting mixture was adjusted by nitric acid solution or sodium hydroxide solution under vigorous stirring to a certain pH value. The mixture was loaded into a 23 mL Teflon-lined autoclave, filled with de-ionized water up to 14 mL and sealed tightly. The autoclaves were kept at 180 °C for 48 h. After cooling to room temperature, the precipitate was collected, washed with de-ionized water and absolute ethanol for several times, and then dried in air at 60 °C.

2.2. Characterizations

X-ray diffraction (XRD) patterns were collected on a Bruker D8 Advance X-ray diffractometer with $\text{CuK}\alpha$ radiation. The accelerating voltage and the applied current were 40 kV and 40 mA, respectively. Data were recorded at a scanning rate of 0.004° 2θ s⁻¹ in the 2θ range of 10–70°. The specific surface area of the samples was measured by nitrogen sorption at 77 K on ASAP 2020 instrument and calculated by the BET method. UV-visible absorption spectra (UV-DRS) of the powders were obtained for the dry-pressed disk samples using a UV-visible spectrophotometer (Cary 500 Scan Spectrophotometers, Varian, USA). BaSO_4 was used as a reflectance standard in the UV-vis diffuse reflectance experiments. The transmission electron microscopy (TEM), high-resolution transmission electron microscopy (HRTEM) images and energy dispersive X-ray spectrum (EDX) were measured by a JEOL model JEM 2010 EX instrument at an accelerating voltage of 200 kV. The powder particles were supported on a carbon film coated on a 3 mm diameter fine-mesh copper grid. A suspension of the sample in ethanol was sonicated and a drop was dripped on the support film. FT-IR spectra were recorded in transmittance mode with a resolution of 4 cm⁻¹ using a Nicolet Nexus 670 FTIR spectrometer and 25 mg of catalyst. Electron spin resonance (ESR) spectra were obtained using Bruker model ESP 300E electron paramagnetic resonance spectrometer equipped with a quanta-Ray Nd:YAG laser system as the irradiation light source ($\lambda = 266$ nm).

2.3. Photocatalytic activity measurements

The photocatalytic activities of the as-prepared samples were investigated by the degradations of methyl orange (MO) and gaseous benzene. Aqueous photocatalytic reactions were performed in a quartz tube with 4.6 cm inner diameter and 17 cm length. Four 4-W UV lamps with a wavelength centered at 254 nm (Philips, TUV 4W/G4 T5) were used as illuminating source. 80 mg of photocatalyst was added into 80 mL of MO solution (10⁻⁵ mol/L) and stirred for 2 h before irradiation to ensure that adsorption/desorption equilibrium had been reached. At given irradiation time intervals, 4 mL of the suspensions were collected, centrifuged, and filtered through a Millipore filter to separate the photocatalyst particles. The degraded solutions of MO were analyzed by a Varian

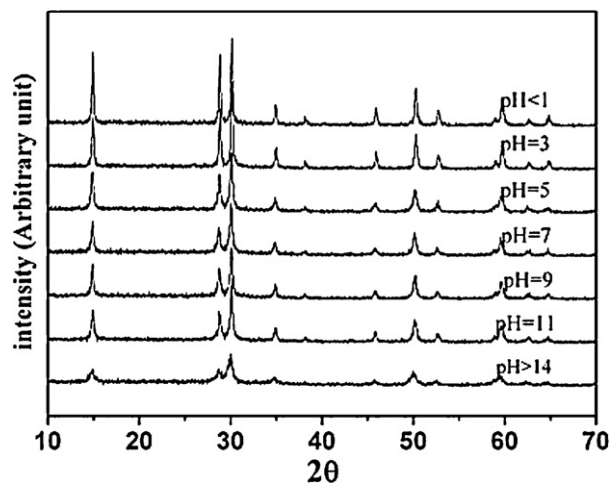


Fig. 1. XRD patterns of products prepared through the hydrothermal process at 180 °C for 48 h under different pH values.

Cary 500 Scan UV-vis spectrophotometer. The absorption peak at 464 nm for MO was monitored. The percentage of degradation is reported as C/C_0 . C is the absorption of MO at each irradiated time interval of the maximum peak of the absorption spectrum at wavelength 464 nm. C_0 is the absorption of the starting concentration when adsorption/desorption equilibrium was achieved.

The photocatalytic degradation of gaseous benzene was conducted in a tubular quartz micro-reactor operating in a continuous-flow mode. The reactor was surrounded by four 4 W UV lamps with wavelength centered at 254 nm. The catalyst loading was 0.3 g (50–70 mesh). Benzene was diluted with oxygen and the resulting gaseous mixture was used to afford a reactant stream. The initial concentrations of benzene and carbon dioxide in the stream were 300 and 0 ppm, respectively. The flow rate of the reactant mixture was kept at 20 mL/min⁻¹. Simultaneous determination of the concentrations of benzene and carbon dioxide was performed with an online gas chromatograph (Agilent 6890N) equipped with a flame ionization detector, a thermal conductivity detector and a Porapak R column. The reaction temperature was controlled at 30 ± 1 °C by a water-cooling system.

2.4. Theoretical calculations

The structural optimizations for $\text{CaSb}_2\text{O}_5(\text{OH})_2$ and cubic $\text{Ca}_2\text{Sb}_2\text{O}_7$ were performed by using the projector-augmented wave (PAW) formalism of density functional theory (DFT), as implemented in the Vienna ab initio simulations package (VASP) [21–23], and the Perdew–Burke–Ernzerhof (PBE) type exchange-correlation was adopted [24]. In the calculations, the volume of cell and positions of all atom were allowed to be relaxed at an energy cutoff of 400 eV and a 5 × 5 × 5 Monkhorst–Pack k -point grid.

3. Results and discussion

Fig. 1 shows the XRD patterns of the products obtained via a hydrothermal treatment of Sb_2O_5 and $\text{Ca}(\text{CH}_3\text{COO})_2$ at 180 °C for 48 h under different pH values. The XRD patterns for products obtained under different pH values are almost similar and is corresponding to one or a mixture of the following three metal oxides: $\text{CaSb}_2\text{O}_5(\text{OH})_2$ (JCPDS card 32-0154), cubic $\text{Ca}_2\text{Sb}_2\text{O}_7$ (JCPDS card 73-1736) and Sb_6O_{13} (JCPDS card 33-1111). To distinguish the real chemical composition of the product obtained, the EDX was used to detect the atomic ratios of Ca and Sb in the products and the results are shown in Table 1. It is found that the atomic ratio of Ca and Sb of the products prepared with pH value range from 3 to 11 is close

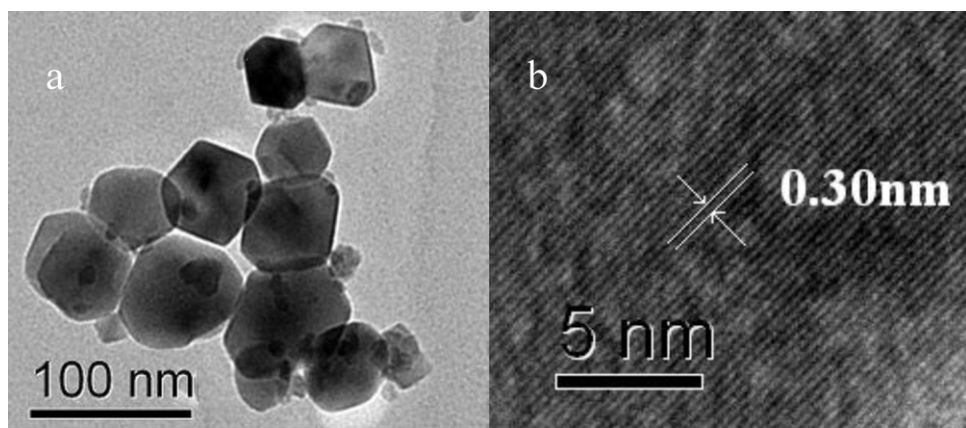


Fig. 2. Images of $\text{CaSb}_2\text{O}_5(\text{OH})_2$ prepared at $\text{pH} = 11$ (a) low magnification TEM image; (b) HRTEM image.

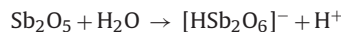
Table 1

Atomic ratios of Ca and Sb for samples prepared under different pH values as calculated from EDX.

Reaction pH value	1	3	5	7	9	11	14
Atomic ratios of Ca to Sb	~1:3.3	~1:2	~1:2	~1:2	~1:2	~1:2	~1:1

to stoichiometrical 1:2 and indicates that the products obtained in this pH range are $\text{CaSb}_2\text{O}_5(\text{OH})_2$ and no impurity coexists. When pH value is 1, the product has a Ca/Sb atomic ratio of about 1:3. This indicates that the product obtained at this pH value may be a mixture of Sb_6O_{13} and $\text{CaSb}_2\text{O}_5(\text{OH})_2$. When the reaction was carried out at strong basic condition ($\text{pH} = 14$ or higher), the obtained product has an atomic ratio of Ca to Sb at about 1:1, which suggests that the obtained product is $\text{Ca}_2\text{Sb}_2\text{O}_7$. Based on these results, the chemical reactions involved in the formation of $\text{CaSb}_2\text{O}_5(\text{OH})_2$ and $\text{Ca}_2\text{Sb}_2\text{O}_7$ can be formulated as following:

Under mild acidic condition,



Under basic condition,



Under extremely basic condition ($\text{pH} \geq 14$),



Under mild acidic or neutral condition, Sb_2O_5 is partly hydrolyzed to give $[\text{HSb}_2\text{O}_6]^-$, while under basic condition, Sb_2O_5 is partly hydrolyzed to give $[\text{Sb}(\text{OH})_6]^-$ [25]. Both anionic $[\text{HSb}_2\text{O}_6]^-$ and $[\text{Sb}(\text{OH})_6]^-$ can react with Ca^{2+} to give $\text{CaSb}_2\text{O}_5(\text{OH})_2$ nuclei, which further grow to give $\text{CaSb}_2\text{O}_5(\text{OH})_2$ nanoparticles. However, under strong acidic condition, the formation of $[\text{HSb}_2\text{O}_6]^-$ is strongly inhibited. Since Sb^{5+} is more stable in high temperature than Sb^{3+} , Sb^{5+} in Sb_2O_5 is partially reduced to Sb^{3+} and therefore Sb_6O_{13} is obtained at a highly acidic condition ($\text{pH} = 1$). Under extremely basic condition, $\text{CaSb}_2\text{O}_5(\text{OH})_2$ can further react with HO^- to give $\text{Ca}_2\text{Sb}_2\text{O}_7$. Although a stoichiometric 1:2 of Ca to Sb atomic ratio is required to give $\text{CaSb}_2\text{O}_5(\text{OH})_2$, the reaction between Sb_2O_5 and Ca^{2+} in 1:1 ratio still lead to the formation of $\text{CaSb}_2\text{O}_5(\text{OH})_2$ except in the extreme basic condition. The above results indicate that the pH of the reactants plays an important role in the formation of different Ca-Sb oxides. An one-pot facile reaction of Sb_2O_5 and Ca^{2+} can controllably lead to nanocrystalline $\text{CaSb}_2\text{O}_5(\text{OH})_2$ and $\text{Ca}_2\text{Sb}_2\text{O}_7$ by simply changing the pH of the reaction mixture.

TEM image of $\text{CaSb}_2\text{O}_5(\text{OH})_2$ prepared at pH value of 11 reveals that the sample consist mainly of irregular nanoparticles with size in the range of 20–60 nm (Fig. 2a). The HRTEM image shows clear lattice fringes and the fringes of $d = 0.30$ nm match that of the (2 2 2) plane of $\text{CaSb}_2\text{O}_5(\text{OH})_2$ (Fig. 2b). However, the as-prepared $\text{Ca}_2\text{Sb}_2\text{O}_7$ (sample obtained at pH value of 14) shows a totally different morphology (Fig. 3a). The TEM image of $\text{Ca}_2\text{Sb}_2\text{O}_7$ shows that

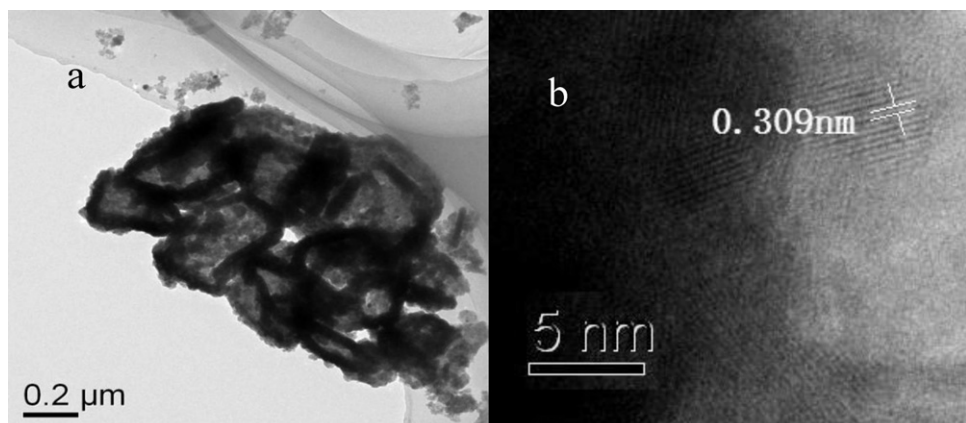


Fig. 3. Images of cubic $\text{Ca}_2\text{Sb}_2\text{O}_7$ (a) low magnification TEM image; (b) HRTEM image.

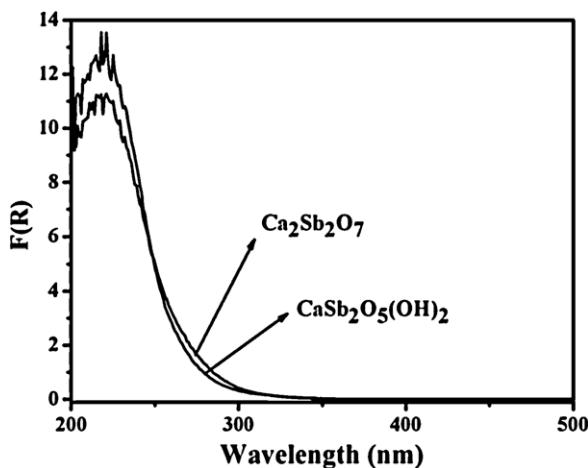


Fig. 4. UV-vis DRS of $\text{CaSb}_2\text{O}_5(\text{OH})_2$ prepared at pH = 11 and cubic $\text{Ca}_2\text{Sb}_2\text{O}_7$.

the sample is consist of rectangular shaped nanostructures in the dimension of 300–400 nm. As evidenced in the TEM image, these rectangular shaped nanostructures have thick rim and relatively thin center and are assembled by small nanoparticles. The HRTEM image shows clear lattice fringes of $d = 0.309$ nm, corresponding to the (3 1 1) plane of cubic $\text{Ca}_2\text{Sb}_2\text{O}_7$ (Fig. 3b).

The band gaps of $\text{CaSb}_2\text{O}_5(\text{OH})_2$ and $\text{Ca}_2\text{Sb}_2\text{O}_7$ were determined based on the UV-vis DRS. The wavelength at the absorption edge, λ , is determined as the intercept on the wavelength axis for a tangent line drawn on the absorption spectra. By applying this method,

the absorption edges for $\text{CaSb}_2\text{O}_5(\text{OH})_2$ and $\text{Ca}_2\text{Sb}_2\text{O}_7$ can be determined to be ca. 270 nm and 275 nm, corresponding to the band gap of 4.6 eV and 4.5 eV respectively (Fig. 4).

The photocatalytic activity of $\text{CaSb}_2\text{O}_5(\text{OH})_2$ prepared at pH 11 and cubic $\text{Ca}_2\text{Sb}_2\text{O}_7$ was evaluated by the degradations of aqueous MO and gaseous benzene under UV light irradiations. Temporal changes in the concentration of MO as monitored by the maximal absorption in UV-vis spectra at 464 nm over $\text{CaSb}_2\text{O}_5(\text{OH})_2$ and $\text{Ca}_2\text{Sb}_2\text{O}_7$ are shown in Fig. 5a. It was found that a total degradation of MO was achieved over irradiated $\text{CaSb}_2\text{O}_5(\text{OH})_2$ in 60 min, comparable to that over commercial Degussa P25. $\text{Ca}_2\text{Sb}_2\text{O}_7$ showed a little lower photocatalytic activity and about 70% of MO was degraded in a similar illuminated period. On the contrary, only about 10% of MO was degraded with pure UV irradiations, indicating that both $\text{CaSb}_2\text{O}_5(\text{OH})_2$ and $\text{Ca}_2\text{Sb}_2\text{O}_7$ are photocatalytic active. Besides this, both $\text{CaSb}_2\text{O}_5(\text{OH})_2$ and $\text{Ca}_2\text{Sb}_2\text{O}_7$ show high stability during the photocatalytic reactions and no obvious loss of photocatalytic activity was observed in five photocatalytic runs (Fig. 5b).

The photocatalytic degradation of gaseous benzene was also evaluated over $\text{CaSb}_2\text{O}_5(\text{OH})_2$ (obtained at pH 11) and $\text{Ca}_2\text{Sb}_2\text{O}_7$. The conversion of benzene and the amount of the produced CO_2 over $\text{CaSb}_2\text{O}_5(\text{OH})_2$ and $\text{Ca}_2\text{Sb}_2\text{O}_7$ as a function of illuminations time reveals that $\text{CaSb}_2\text{O}_5(\text{OH})_2$ also shows a superior photocatalytic performance in the degradation of benzene as compared to $\text{Ca}_2\text{Sb}_2\text{O}_7$ (Fig. 6a and b). The conversion of benzene over $\text{CaSb}_2\text{O}_5(\text{OH})_2$ is about 7.5% and about 130 ppm of CO_2 is produced, corresponding to an almost 100% mineralization ratio. However, the conversion ratio of benzene over $\text{Ca}_2\text{Sb}_2\text{O}_7$ is only about 5% and the amount of the produced CO_2 is about 50 ppm,

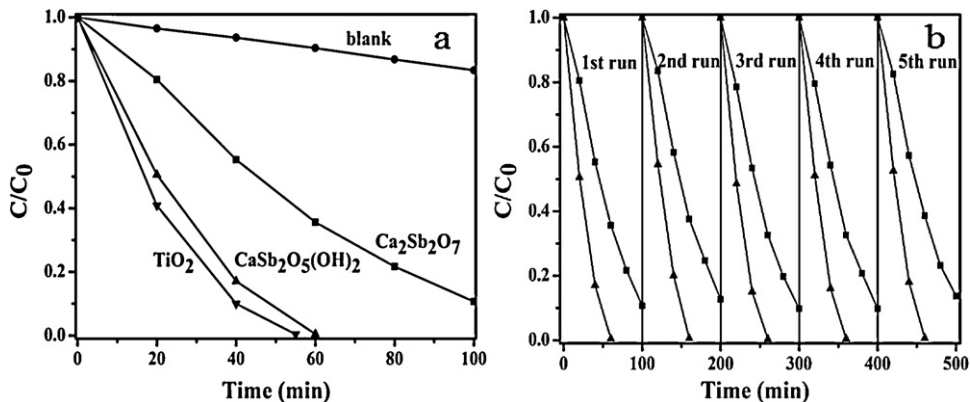


Fig. 5. (a) Temporal changes of MO concentration as monitored by the UV-vis absorption spectra at 464 nm over irradiated $\text{CaSb}_2\text{O}_5(\text{OH})_2$, cubic $\text{Ca}_2\text{Sb}_2\text{O}_7$, P25 and UV irradiations only; (b) cycling runs in the photocatalytic degradations of MO over $\text{CaSb}_2\text{O}_5(\text{OH})_2$ and cubic $\text{Ca}_2\text{Sb}_2\text{O}_7$.

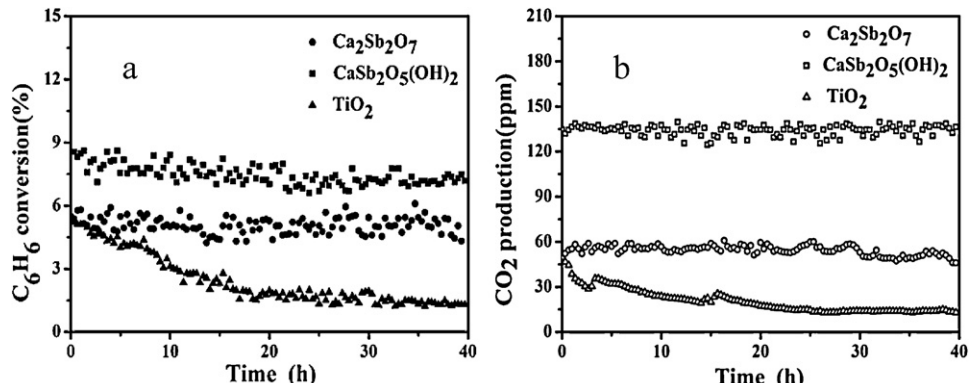


Fig. 6. Photocatalytic degradation of C_6H_6 over $\text{CaSb}_2\text{O}_5(\text{OH})_2$ prepared at pH = 11, cubic $\text{Ca}_2\text{Sb}_2\text{O}_7$ and P25 as a function of irradiations time. (a) Conversion of C_6H_6 ; (b) amounts of produced CO_2 .

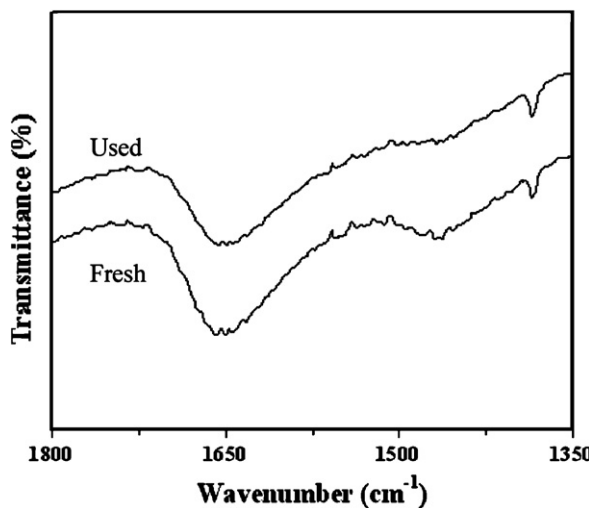


Fig. 7. FT-IR spectra of $\text{CaSb}_2\text{O}_5(\text{OH})_2$ prepared at $\text{pH} = 11$ before and after the photocatalytic degradation of benzene.

which corresponds to an almost 50% mineralization of benzene. Although the initial conversion ratio of benzene over P25 is also 5.0%, it gradually decreases to about 1.3% with time on stream and only a small amount of CO_2 (ca. 15 ppm) is produced (Fig. 6a and b). Unlike P25, both $\text{CaSb}_2\text{O}_5(\text{OH})_2$ and $\text{Ca}_2\text{Sb}_2\text{O}_7$ are quite stable during the whole photocatalytic reaction (40 h) without noticeable deactivation. The stability of the catalysts is also confirmed by the almost similar FT-IR spectra of the catalysts before and after the photocatalytic reaction, indicating that no polymerized products have been deposited in the surface of the catalysts during the photocatalytic reaction (Fig. 7). Our previous result has indicated that the capability of maintaining a clean surface of the photocatalysts during benzene degradation is a result of a preferential HO radical mediated route for the benzene degradation [26]. Indeed, the generation of both $\text{O}_2^{\bullet-}$ and OH^{\bullet} radicals over the irradiated $\text{CaSb}_2\text{O}_5(\text{OH})_2$ and $\text{Ca}_2\text{Sb}_2\text{O}_7$ has been confirmed by the ESR spin-trap with DMPO technique (Fig. 8a and b).

The above results show that $\text{CaSb}_2\text{O}_5(\text{OH})_2$ are more active than cubic $\text{Ca}_2\text{Sb}_2\text{O}_7$ in both the photocatalytic degradation of MO and benzene. It is generally believed that the photocatalytic performance of the semiconductor photocatalysts is influenced by factors like band gap, specific surface area, electronic structure and crystal structure. Since $\text{CaSb}_2\text{O}_5(\text{OH})_2$ and cubic $\text{Ca}_2\text{Sb}_2\text{O}_7$ has comparable band gap (4.6 eV for $\text{CaSb}_2\text{O}_5(\text{OH})_2$ vs. 4.5 eV for cubic $\text{Ca}_2\text{Sb}_2\text{O}_7$), and the as-prepared $\text{Ca}_2\text{Sb}_2\text{O}_7$ possesses a higher specific surface area ($31.2 \text{ m}^2/\text{g}$) than that of $\text{CaSb}_2\text{O}_5(\text{OH})_2$ ($21.6 \text{ m}^2/\text{g}$), the superior photocatalytic performance of $\text{CaSb}_2\text{O}_5(\text{OH})_2$ as compared to

that of cubic $\text{Ca}_2\text{Sb}_2\text{O}_7$ cannot be attributed to their different band gaps and their different specific surface area. To elucidate the factors that may contribute to the higher photocatalytic activity of $\text{CaSb}_2\text{O}_5(\text{OH})_2$, the electronic structure as well as the crystal structure of $\text{CaSb}_2\text{O}_5(\text{OH})_2$ and $\text{Ca}_2\text{Sb}_2\text{O}_7$ are compared.

To analyze the electronic structure, we have carried out density functional theory (DFT) calculations for $\text{CaSb}_2\text{O}_5(\text{OH})_2$ and cubic $\text{Ca}_2\text{Sb}_2\text{O}_7$. Fig. 9 presents the calculated band structures and density of states (DOS) of $\text{CaSb}_2\text{O}_5(\text{OH})_2$ and cubic $\text{Ca}_2\text{Sb}_2\text{O}_7$, in which the zero energy value is set at the top of the valence band to easily identify the band gap and the relative position of the states. For $\text{CaSb}_2\text{O}_5(\text{OH})_2$, an indirect transition from the valence band at the point near W to the conduction band at Γ point as the minimum band gap, for which a value of 1.30 eV is determined. Due to the inherent deficiency of the DFT method, the calculated band gap is smaller than the experimental value (4.6 eV) [27]. According to the DOS of $\text{CaSb}_2\text{O}_5(\text{OH})_2$ shown in Fig. 9(b) and (c), the valence bands (VB) appeared in the range between -9.4 and 0.0 eV are mainly derived from O 2p states, and some obvious components of the 5s/5p states of Sb atom also can be found in the same region. For the conduction band (CB), it is dominated by the 5s states of the Sb atom in the region between 1.3 eV and 5.0 eV. While for the $\text{Ca}_2\text{Sb}_2\text{O}_7$, it can be seen clearly that a direct band gap was found at Γ point (Fig. 9d). The predicted band gap of $\text{Ca}_2\text{Sb}_2\text{O}_7$ is 0.29 eV which is reducing the band gap (1.01 eV) as compared to the $\text{CaSb}_2\text{O}_5(\text{OH})_2$. Examining the PDOS shown in Fig. 9(e) and (f), the main components of conduction band minimum (CBM) and valence band maximum (VBM) of $\text{Ca}_2\text{Sb}_2\text{O}_7$ are still mainly originated from Sb 5s and O 2p orbitals. Therefore, it seems that $\text{CaSb}_2\text{O}_5(\text{OH})_2$ and cubic $\text{Ca}_2\text{Sb}_2\text{O}_7$ does not show much difference on those energy bands near the CBM and VBM regions. Therefore it is possible that the different photocatalytic performance between $\text{CaSb}_2\text{O}_5(\text{OH})_2$ and $\text{Ca}_2\text{Sb}_2\text{O}_7$ may be related to their different crystal structures.

Although $\text{CaSb}_2\text{O}_5(\text{OH})_2$ and cubic $\text{Ca}_2\text{Sb}_2\text{O}_7$ both crystallize in $Fd\text{-}3m$ space group, their structures are quite different. The structure of $\text{CaSb}_2\text{O}_5(\text{OH})_2$ can be described as distorted Sb_6O_6 octahedra sharing their corners with six surrounding Sb_6O_6 octahedra with Ca^{2+} and OH^- placed in the interstitials among the Sb_6O_6 octahedra, while cubic $\text{Ca}_2\text{Sb}_2\text{O}_7$ is made up from Sb_8 polyhedra sharing their edge with surrounding Sb_8 polyhedra, with Ca^{2+} locates in the interstitials of Sb_8 polyhedra. Recently, based on a survey of a series of inorganic oxides consisting of d^{10} and d^0 cations, a model for the evaluation of the photocatalytic activity has been proposed for the tunnel-structure semiconductor photocatalysts [17,28]. According to this model, there exists a correlation between the crystal packing factor (PF) and the photocatalytic activity of the tunnel-structure photocatalysts. A lower PF is correlated with

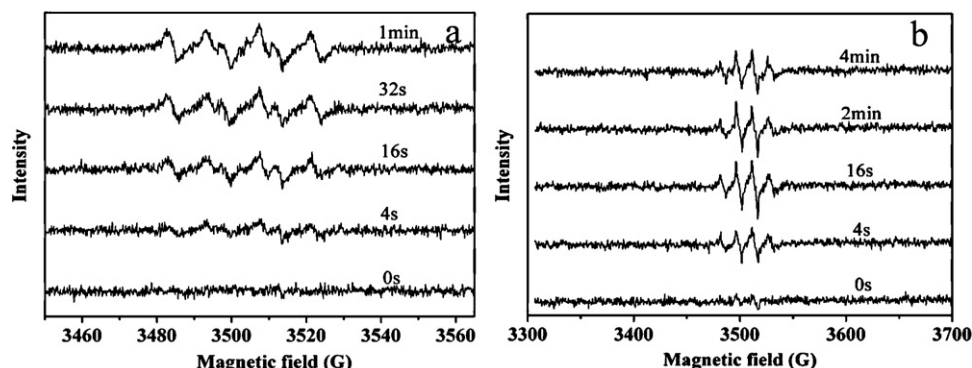


Fig. 8. DMPO spin-trapping ESR spectra of $\text{CaSb}_2\text{O}_5(\text{OH})_2$ prepared at $\text{pH} = 11$ system with and without irradiations (a) in methanol dispersion for $\text{DMPO-O}_2^{\bullet-}$; (b) in aqueous dispersion for DMPO-OH^{\bullet} .

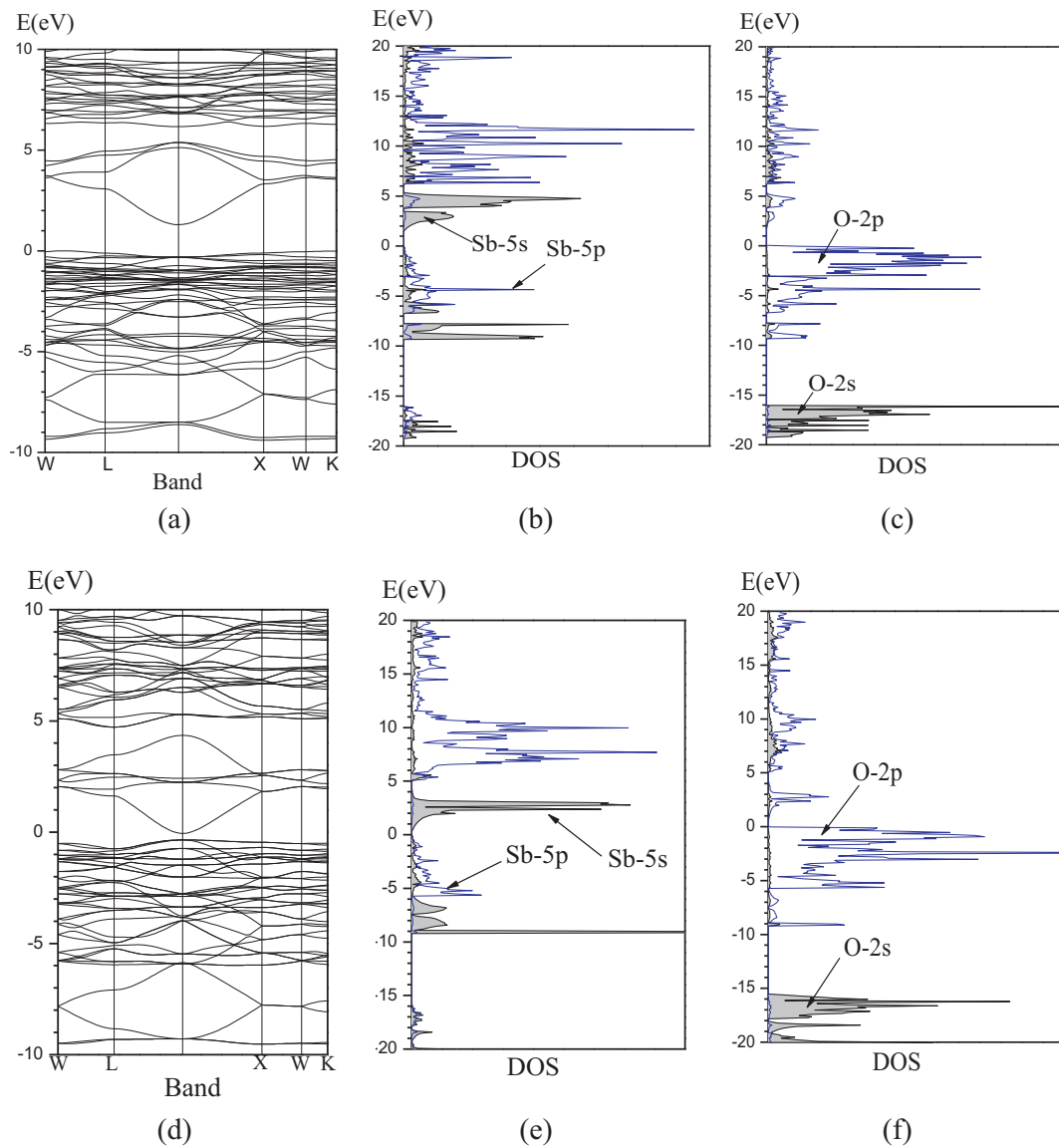


Fig. 9. $\text{CaSb}_2\text{O}_5(\text{OH})_2$ (a) band structure, (b) some partial DOSs of Sb and (c) oxygen atom connected with Sb. (d) Band structure, some partial DOSs of (e) Sb and (f) oxygen atom connected with Sb for cubic $\text{Ca}_2\text{Sb}_2\text{O}_7$. In the figures, the valence-band maximum is taken as the energy zero.

a higher electron–hole separation and transportation, and would results in better photocatalytic activity. The calculations of the PF of $\text{CaSb}_2\text{O}_5(\text{OH})_2$ and cubic $\text{Ca}_2\text{Sb}_2\text{O}_7$ based on their crystal structures reveals that the PF of $\text{CaSb}_2\text{O}_5(\text{OH})_2$ (62.55%) is lower than that of cubic $\text{Ca}_2\text{Sb}_2\text{O}_7$ (64.62%). According to this model, the lower PF of $\text{CaSb}_2\text{O}_5(\text{OH})_2$ is probably responsible for its higher photocatalytic activity as compared to cubic $\text{Ca}_2\text{Sb}_2\text{O}_7$.

4. Conclusion

In summary, depending on the reaction pH, $\text{CaSb}_2\text{O}_5(\text{OH})_2$ and cubic $\text{Ca}_2\text{Sb}_2\text{O}_7$ with large specific surface area were controlled synthesized from Sb_2O_5 via a facile hydrothermal method. $\text{CaSb}_2\text{O}_5(\text{OH})_2$ show higher photocatalytic activity than cubic $\text{Ca}_2\text{Sb}_2\text{O}_7$ in the degradation of MO and benzene. A lower packing factor (PF) of $\text{CaSb}_2\text{O}_5(\text{OH})_2$ contributes to its higher photocatalytic activity. Further studies on the preparations and photocatalytic activity of other antimonate photocatalysts are still going on in our lab.

Acknowledgments

The work was supported by National Natural Science Foundation of China (20977016, 21073035, 90922022), National Basic Research Program of China (973 Program: 2011CB612314). The Award Program for Minjiang Scholar Professorship to Z. Li is also acknowledged.

References

- [1] M.R. Hoffmann, S.T. Martin, W. Choi, D.W. Bahnemann, Chemical Reviews 95 (1995) 69–96.
- [2] A. Fujishima, T.N. Rao, D.A. Tryk, Journal of Photochemistry and Photobiology C 1 (2000) 1–21.
- [3] C.C. Chen, W.H. Ma, J.C. Zhao, Chemical Society Reviews 39 (2010) 4206–4219.
- [4] L. Zhang, W.Z. Wang, L. Zhou, M. Shang, S. Sun, Applied Catalysis B: Environmental 90 (2009) 458–462.
- [5] Z.H. Ai, L.Z. Zhang, S.C. Lee, Journal of Physical Chemistry C 114 (2010) 18594–18600.
- [6] Z. Bian, Y. Huo, Y. Zhang, J. Zhu, Y. Lu, H. Li, Applied Catalysis B: Environmental 91 (2009) 247–253.

- [7] X. Zhu, J. Zhang, F. Chen, *Applied Catalysis B: Environmental* 102 (2011) 316–322.
- [8] S. Zhu, T. Xu, H. Fu, J. Zhao, Y. Zhu, *Environmental Science and Technology* 41 (2007) 6234–6239.
- [9] Z. Yi, J. Ye, N. Kikugawa, T. Kako, S. Ouyang, H. Stuart-Williams, H. Yang, J. Cao, W. Lou, Z. Li, Y. Liu, R.L. Withers, *Nature Materials* 9 (2010) 559–564.
- [10] P. Wang, B.B. Huang, X.Y. Qin, X.Y. Zhang, Y. Dai, J.Y. Wei, M.H. Whangbo, *Angewandte Chemie International Edition* 47 (2008) 7931–7933.
- [11] C. Hu, T.W. Peng, X.X. Hu, Y.L. Nie, X.F. Zhou, J.H. Qu, H. He, *Journal of the American Chemical Society* 132 (2010) 857–862.
- [12] X.P. Lin, F.Q. Huang, W.D. Wang, Y.M. Wang, Y.J. Xia, J.L. Shi, *Applied Catalysis A: General* 313 (2006) 213–218.
- [13] H. Xue, Z.H. Li, L. Wu, Z.X. Ding, X.X. Wang, X.Z. Fu, *Journal of Physical Chemistry C* 112 (2008) 5850–5855.
- [14] K.L. Zhang, X.P. Lin, F.Q. Huang, Y.M. Wang, *Journal of Molecular Catalysis A: Chemical* 258 (2006) 185–190.
- [15] X.P. Lin, F.Q. Huang, W.D. Wang, K.L. Zhang, *Applied Catalysis A: General* 307 (2006) 257–262.
- [16] Q.Q. You, Y.H. Fu, Z.X. Ding, L. Wu, X. Wang, Z.H. Li, *Dalton Transactions* 40 (2011) 5774–5780.
- [17] X. Lin, J. Wu, X. Lv, Z. Shan, W. Wang, F. Huang, *Physical Chemistry Chemical Physics* 11 (2009) 10047–10052.
- [18] W.J. Liu, P.Y. Lin, H. Jin, H. Xue, Y.F. Zhang, Z.H. Li, *Journal of Molecular Catalysis A: Chemical* 349 (2011) 80–85.
- [19] M. Sun, D.Z. Li, Y. Chen, W. Chen, W. Li, Y. He, X.Z. Fu, *Journal of Physical Chemistry C* 113 (2009) 13825–13831.
- [20] M. Abe, *Bulletin of the Chemical Society of Japan* 52 (1979) 1386.
- [21] G. Kresse, J. Furthmüller, *Computation Materials Science* 6 (1996) 15–50.
- [22] G. Kresse, J. Furthmüller, *Physical Review B* 54 (1996) 11169–11186.
- [23] G. Kresse, J. Hafner, *Physical Review B* 47 (1993) 558–561.
- [24] J.P. Perdew, K. Burke, M. Ernzerhof, *Physical Review Letters* 77 (1996) 3865–3868.
- [25] S.H. Gate, E. Richardson, *Journal of Inorganic and Nuclear Chemistry* 23 (1961) 257–263.
- [26] Z.H. Li, Z.P. Xie, Y.F. Zhang, L. Wu, X.X. Wang, X.Z. Fu, *Journal of Physical Chemistry C* 111 (2007) 18348–18352.
- [27] Z. Li, H. Dong, Y. Zhang, T. Dong, X. Wang, J. Li, X. Fu, *Journal of Physical Chemistry C* 112 (2008) 16046–16051.
- [28] J. Wu, F. Huang, Z. Shan, Y. Wang, *Dalton Transactions* 40 (2011) 6906–6911.